



HAL
open science

Cr/B4C multilayer mirrors: Study of interfaces and X-ray reflectance

C Burcklen, R Soufli, D Denetiere, F Polack, B Capitanio, E Gullikson, E Meltchakov, M Thomasset, A Jérôme, Sébastien de Rossi, et al.

► **To cite this version:**

C Burcklen, R Soufli, D Denetiere, F Polack, B Capitanio, et al.. Cr/B4C multilayer mirrors: Study of interfaces and X-ray reflectance. *Journal of Applied Physics*, 2016, 119 (12), pp.125307. 10.1063/1.4944723 . hal-04347399

HAL Id: hal-04347399

<https://hal.science/hal-04347399>

Submitted on 15 Dec 2023

HAL is a multi-disciplinary open access archive for the deposit and dissemination of scientific research documents, whether they are published or not. The documents may come from teaching and research institutions in France or abroad, or from public or private research centers.

L'archive ouverte pluridisciplinaire **HAL**, est destinée au dépôt et à la diffusion de documents scientifiques de niveau recherche, publiés ou non, émanant des établissements d'enseignement et de recherche français ou étrangers, des laboratoires publics ou privés.

Cr/B4C multilayer mirrors: Study of interfaces and X-ray reflectance

C. Burcklen, R. Soufli, D. Denetiere, F. Polack, B. Capitanio, E. Gullikson, E. Meltchakov, M. Thomasset, A. Jérôme, S. de Rossi, and F. Delmotte

Citation: *Journal of Applied Physics* **119**, 125307 (2016); doi: 10.1063/1.4944723

View online: <http://dx.doi.org/10.1063/1.4944723>

View Table of Contents: <http://scitation.aip.org/content/aip/journal/jap/119/12?ver=pdfcov>

Published by the [AIP Publishing](#)

Articles you may be interested in

[Reflectivity and structural evolution of Cr/Sc and nitrogen containing Cr/Sc multilayers during thermal annealing](#)
J. Appl. Phys. **104**, 063516 (2008); 10.1063/1.2980051

[Effect of interface treatment with assisted ion beam on Mo-Si multilayer formation for mask blanks for extreme ultraviolet lithography](#)

J. Vac. Sci. Technol. B **25**, 1554 (2007); 10.1116/1.2768604

[B/Si multilayers for soft x-ray and extreme ultraviolet optics](#)

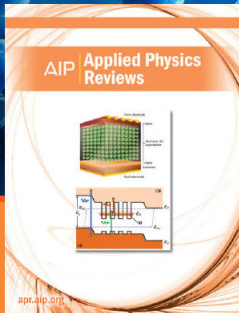
J. Appl. Phys. **89**, 1145 (2001); 10.1063/1.1322590

[Thermal stability of 2.4 nm period Ni-Nb/C multilayer x-ray mirror](#)

Appl. Phys. Lett. **77**, 3654 (2000); 10.1063/1.1328761

[Aging effect of Co/C soft x-ray multilayer mirrors](#)

J. Appl. Phys. **81**, 184 (1997); 10.1063/1.363839



NEW Special Topic Sections

NOW ONLINE
Lithium Niobate Properties and Applications:
Reviews of Emerging Trends

AIP | Applied Physics Reviews

Cr/B₄C multilayer mirrors: Study of interfaces and X-ray reflectance

C. Burcklen,¹ R. Soufli,^{1,2} D. Denetiere,³ F. Polack,³ B. Capitanio,³ E. Gullikson,⁴ E. Meltchakov,¹ M. Thomasset,³ A. Jérôme,¹ S. de Rossi,¹ and F. Delmotte¹

¹Laboratoire Charles Fabry, Institut d'Optique Graduate School, CNRS, Université Paris-Saclay, 91127 Palaiseau Cedex, France

²Lawrence Livermore National Laboratory, 7000 East Avenue, Livermore, California 94550, USA

³Synchrotron SOLEIL, L'Orme des Merisiers, Saint Aubin, BP 48F-91192 Gif sur Yvette Cedex, France

⁴Center for X-ray Optics, Lawrence Berkeley National Laboratory, 1 Cyclotron Rd., Berkeley, California 94720, USA

(Received 23 November 2015; accepted 10 March 2016; published online 24 March 2016)

We present an experimental study of the effect of layer interfaces on the x-ray reflectance in Cr/B₄C multilayer interference coatings with layer thicknesses ranging from 0.7 nm to 5.4 nm. The multilayers were deposited by magnetron sputtering and by ion beam sputtering. Grazing incidence x-ray reflectometry, soft x-ray reflectometry, and transmission electron microscopy reveal asymmetric multilayer structures with a larger B₄C-on-Cr interface, which we modeled with a 1–1.5 nm thick interfacial layer. Reflectance measurements in the vicinity of the Cr L_{2,3} absorption edge demonstrate fine structure that is not predicted by simulations using the currently tabulated refractive index (optical constants) values for Cr. © 2016 AIP Publishing LLC. [<http://dx.doi.org/10.1063/1.4944723>]

I. INTRODUCTION

Metal/B₄C multilayer interference coatings, deposited as part of high-efficiency reflective or diffractive optics (e.g., mirrors and gratings), are relevant for a wide range of applications covering the spectral range from the extreme ultraviolet (EUV) to hard x-rays, including synchrotron optics,¹ astronomy,^{2,3} next-generation photolithography,⁴ etc. In the spectral range between the Si L_{2,3}-edge and the B K-edge (100 eV < E < 180 eV), B₄C is often used as the “spacer” material in multilayer coatings. Proposed combinations include Mo/B₄C,^{5,6} La/B₄C,^{5–8} Ru/B₄C,⁹ and Pd/B₄C.¹⁰ At higher energies (typically E > 500 eV), short-period multilayer mirrors are required, and B₄C is often used as a substitute to C because it provides smoother layer interfaces and higher reflectance values.^{11–13} Common multilayer material pairs for this spectral domain are W/B₄C,^{2,3,11,14} Ni/B₄C, or Mo/B₄C,^{7,15} but other combinations have been reported as well, for example, Fe/B₄C and Rh/B₄C.¹¹ B₄C has also been used in the EUV domain (E < 100 eV), as for instance in Si/B₄C,¹⁶ Si/Mo/B₄C,¹⁷ or Al/Mo/B₄C¹⁸ multilayers.

Experimental results with Cr/B₄C multilayer mirrors have been reported for applications such as synchrotron optics for x-rays of intermediate energies (1–3 keV)¹⁹ or to reflect the B-K α line near 183 eV.⁶ B₄C thin layers have also been introduced as barrier layers in Cr-based multilayers, such as Cr/Sc or Cr/V.^{20–22} Moreover, promising designs have been reported using Cr/B₄C multilayers, for instance, narrowband mirrors near the Cr K-edge²³ and broadband mirrors with aperiodic multilayers.²⁴ Cr/B₄C is also an attractive candidate material pair for mirrors operating at photon energies just below the Cr L_{2,3}-edge, due to the reduced Cr absorption which leads to enhanced reflectance. Another advantage of Cr/B₄C multilayers is thin film stress manipulation. By optimizing layer thickness and deposition parameters, it should be possible to produce very low stress

coatings by compensating the B₄C compressive stress with the Cr tensile stress.²⁵

Despite the potential interest of this material combination, very few studies on Cr/B₄C multilayer structures and their interfaces have been reported up to now. A comparison of ultrathin metal/light material multilayers was published in 2002 and includes a Cr/B₄C multilayer deposited by magnetron sputtering (MS).¹³ The authors studied the film microstructure by transmission electron microscopy (TEM) and interpreted their results by means of thermodynamic and thermochemical considerations. However, no experimental results concerning the x-ray reflective performance and its dependence on layer interfaces in this multilayer have been reported.

In this paper, we present an experimental study and optimization of Cr/B₄C multilayers deposited by magnetron sputtering and by ion beam sputtering (IBS). Characterization methods include grazing incidence x-ray reflectometry (GIXR) using a Cu-K α source, soft x-ray reflectometry (SXR) using synchrotron sources, TEM, and atomic force microscopy (AFM). We propose a model with an additional interdiffusion layer at the B₄C-on-Cr interface (3-layer model) in order to interpret the reflectometry results consistently among different samples measured at different photon energies. Then, we present TEM images of selected Cr/B₄C samples and compare them with the proposed 3-layer model. Finally, we report on measurements of Cr/B₄C reflectance in the vicinity of the Cr L_{2,3} edge and compare them with simulations using available optical constants.

II. EXPERIMENTAL PART

A. Equipment

The multilayer samples discussed in this paper have been deposited by IBS or by MS. Concerning the IBS deposition system, the residual pressure is in the range 10^{−6} Pa, and the Ar working pressure is 4 × 10^{−2} Pa. A 3 cm Ion Tech

gun delivers the ion beam to the target. The multilayer deposition is achieved by rotating the bulk material targets facing the sample holder. The chamber geometry is described in more detail in Ref. 26. Float glass substrates (with 20 mm diameter and 3 mm thickness) were used in the IBS depositions. The MS deposition system is a Plassys MP800S that has been described in previous papers.¹⁷ During the deposition process, the Ar working gas pressure was 0.093 Pa in the deposition chamber. The plasma discharge was established with an 150 W RF power for the B₄C target and 50 mA DC current (16 W) for the Cr target. Si wafer substrates of 100 orientation and 1 mm thickness were used in the MS depositions, with dimensions 25 × 25 mm². For both machines (IBS and MS), we estimated the deposition rate of each material by depositing and characterizing single-layer thin films of the material, prior to multilayer deposition. During multilayer deposition, the thickness of each layer is controlled by the deposition time. All multilayer structures are characterized by means of grazing-incidence X-ray reflectometry at 0.154 nm. Our GIXR apparatus consists of a commercial grazing incidence reflectometer (BRUKER[®] Discover D8) equipped with a Cu K α radiation source (wavelength $\lambda = 0.154$ nm), a collimating Göbel mirror, a rotary absorber, Soller and divergence slits, and a scintillator.

The Metrology and Tests beamline at Synchrotron SOLEIL and the reflectometer facility at beamline 6.3.2. of the Advanced Light Source (ALS) synchrotron at Lawrence Berkeley National Laboratory (LBNL) provided soft x-ray reflectance measurements in the energy range 150–620 eV.

The Metrology and Tests beamline at Soleil is a versatile soft X-ray beamline for precision at-wavelength metrology.²⁷ The measurements presented here are obtained with the reflectometer of the EUV branch. Bending magnet radiation is monochromatized with a fixed-deviation, plane-grating monochromator. The Au-coated, 75 lines/mm grating is used for measurements around 172 eV. Diffuse scattering as well as the second harmonic of the monochromator are filtered with 0.7 μ m-thick C filter. Higher harmonics are suppressed by a 3 mirror low pass filter using its Cr-coated slot. Both the entrance and output mirrors are set at an incidence angle of 2.8°, and the middle one is at 5.6° incidence angle. The beam is focused on the sample by a spherical entrance mirror. The 3.3 m focal length of this mirror allows for a low angle spread of the Bragg peaks. The base pressure inside the reflectometer is 6×10^{-5} Pa. The energy calibration was done measuring the B K absorption edge of a 0.4 μ m-thick B filter with a 0.1 eV repeatability. The signal was measured using a Zr-coated Si diode, and the background noise was reduced using a 2 mm × 5 mm W slit.

The general characteristics of the ALS reflectometer have been described in detail earlier.^{28,29} The base pressure in the sample chamber is 1.33×10^{-5} Pa. Second harmonic and stray light suppression is achieved with an appropriate transmission filter. When third or higher-order harmonic suppression is needed, an “order suppressor” consisting of three mirrors at a variable grazing incidence angle (depending on energy range) and based on the principle of total external reflection is used in addition to the filters. The ALS storage ring current is used to normalize the signal against the

storage ring current decay. Photon energy calibration is based on the absorption edge of an appropriate filter (Si or Ti L_{2,3} edge, in this work) with relative accuracy of 0.011% rms and with 0.007% repeatability. The reflectance measurements near 172 eV discussed in Section III B were obtained with a 200 lines/mm monochromator grating, a B filter for second-harmonic suppression, and the order suppressor consisting of three C mirrors at 6.5° grazing angle. The reflectance measurements at photon energies in the vicinity of the Cr L_{2,3} edge (540–620 eV) discussed in Section III D were obtained with a 1200 lines/mm monochromator grating, a Co filter for second-harmonic suppression, and the order suppressor consisting of three Ni mirrors at 6.5° grazing angle. A 2-mm-diameter slit was also installed in front of the reflectometer chamber, to reduce scattering from the 1200 lines/mm grating. An additional correction related to scattering from the 1200 lines/mm grating, corresponding to 2% (relative) as determined earlier in Ref. 30, was applied to the reflectance measurements discussed in Section III D. In all ALS measurements in this paper, the signal was collected with a Si photodiode detector with an acceptance angle of 2.4°. Surface roughness measurements were performed at the SOLEIL facility with an Atomic Force Microscope from the Park Company (NX20) in intermittent mode (similar to tapping mode) using AC160 TS Olympus tips.

TEM measurements were performed at EAG Labs (Sunnyvale, California). Prior to TEM imaging, the samples were coated with a ≈ 2 μ m-thick Pt layer for protection purposes and were prepared by Focused Ion Beam (FIB). TEM imaging was performed with a Tecnai TF20 instrument with a field emission gun and 0.2 nm spatial resolution. Bright field images were obtained by selecting the central diffraction order only. High-resolution images were obtained at higher magnifications, by using all the orders in the diffraction pattern. Scanning Transmission Electron Microscopy (STEM) images were also obtained, to show the Z-contrast across the layers. A High Angle Annular Dark Field (HAADF) detector mapped the scattered angles from different materials in each sample. It should be noted that high-Z materials appear bright in STEM (opposite to the TEM bright-field and high-resolution imaging modes).

B. Fitting of GIXR and SXR data

The simulation and fitting of GIXR and SXR data were done using LEPTOS (Bruker commercial software) and IMD software.³¹ The optical constants (δ and β) that were used for the different materials and at several photon energies are gathered in Table I. The complex refractive index (n) is given by: $n = 1 - \delta + i \times \beta$. For Cr, we used the optical constants from the Henke tables.³³ For B₄C and SXR, we used the optical constants of sputtered boron carbide measured by Soufli *et al.*³² For B₄C and GIXR, we used the optical constants calculated from the Henke tables at 8 keV for sputtered boron carbide of the same composition and density, as described in Ref. 32. We have also used interfacial layers (ILs) in the fitting models. We used either the IMD graded interface model³¹ with one interfacial layer (IL-1) or an IL with a modified composition (IL-2). The optical constants of

TABLE I. Material optical constants used for simulation and fitting.

Material	δ at 8052 eV	β at 8052 eV	δ at 170 eV	β at 170 eV	δ at 172.4 eV	β at 172.4 eV
Cr	2.116×10^{-5}	2.162×10^{-6}	0.02460	0.01065	0.02405	0.01026
B ₄ C (Ref. 32)	6.93×10^{-6}	9.27×10^{-9}	0.006883	0.0008266	0.006371	0.0007892
IL-1	1.404×10^{-5}	1.084×10^{-6}	0.01574	0.005739	0.01521	0.005523
IL-2	1.702×10^{-5}	1.536×10^{-6}
B ₂ O ₃	7.733×10^{-6}	2.506×10^{-8}	0.01160	0.002321	0.01114	0.002221

IL-1 and IL-2 are calculated as a weighted average of Cr and B₄C optical constants, with a weight of 50/50 and 70/30, respectively (see Table I). The fitting procedure was the following: The GIXR data were first fitted using the LEPTOS genetic algorithm, the starting point being a Cr/B₄C multilayer coating with the targeted thicknesses for both materials and reasonable interfacial and substrate roughness (0.3 nm). The GIXR experimental noise level was taken into account for the fits. The thickness of each material and the interfacial roughness were optimized in order to fit the GIXR data. Special emphasis was given to the critical angle (position and shape of the curve), the position and the intensity of the Bragg peaks, and the shape of the Kiessig fringes in-between Bragg peaks.

When a satisfying model was obtained at 8 keV, it was then implemented at lower energies with the IMD software and compared to the corresponding SXR data. The model was then manually adjusted (thicknesses and roughnesses), in order to better fit the SXR data, again with special attention on the Bragg peak position and intensity, and on the shape of the Kiessig fringes. A third layer at the B₄C-on-Cr interface was added when needed. After a satisfying model was obtained to fit the SXR data, we tested it again with GIXR data at 8 keV with IMD software. Several iterations were done in this manner, in order to fit consistently both GIXR and SXR measurements. This fitting procedure was repeated until we obtained a model that fitted all measured data for each sample and was also consistent with the model obtained for similar samples.

III. RESULTS AND DISCUSSION

A. GIXR measurements

We deposited six Cr/B₄C multilayer samples with different parameters: samples MS1, MS2, and MS3 by magnetron sputtering and samples IBS1, IBS2, and IBS3 by ion beam sputtering. The number of periods and the targeted layer thickness values for each sample are given in Table II.

TABLE II. List of samples with targeted layer thickness (FG = float glass, NP = number of periods; units = nm).

Sample	Substrate	NP	Cr	B ₄ C	B ₄ C cap
MS1	Si	35	2.5	5.4	...
MS2	Si	10	2.5	5.4	...
MS3	Si	35	2.5	1.08	...
IBS1	FG	10	2.82	3.36	...
IBS2	FG	35	1.87	1.2	1.87
IBS3	FG	35	1.87	0.72	2.35

For all samples, the deposition started with a Cr layer on the substrate and ended with a B₄C layer on top. In some cases, we deposited an additional thickness of B₄C, which is reported in Table II as “B₄C cap,” on top of the last B₄C layer. We measured these 6 samples by GIXR and fitted the experimental data. The GIXR curves measured on the six samples display several orders of well-defined Bragg peaks. This indicates that all six multilayer samples, including those with very small layer thickness, possess a good periodicity and interface quality.

As examples, we show in Fig. 1 the experimental and fitted GIXR curves for samples MS1, MS3, and IBS2. The experimental curves for sample MS1 (Fig. 1(a)) demonstrate up to 9 well-defined Bragg peak orders. One can notice a slight broadening of the high order Bragg peaks (for the 5th and upper orders). This can be attributed to a shift in the multilayer period during the deposition process. We found by simulation that a shift of 2.5 pm/period allows reproducing the experimental Bragg peak widths.

The presence of small peaks around 1.8° and 3° on the experimental curve of Fig. 1(a) corresponds to the 3rd and 5th order Bragg peaks for the Cu-K β line that is not perfectly filtered by the Göbel mirror (the Cu-K β intensity is estimated to be about 1/500 of the Cu-K α).

We report in Table III the fitted parameters for the 6 samples. For MS1, we show the results for 2-layer and 3-layer models that correspond to the curves 1(a) and 1(b), respectively. The model with 2 layers (Cr/B₄C stack) exhibits a significant asymmetry of the multilayer interfaces: the Cr-on-B₄C interface appears very smooth (0.2 nm roughness), whereas the roughness of the B₄C-on-Cr interface is higher (0.6 nm). Such asymmetry in the interfaces has been reported for other metal/B₄C multilayers, such as La/B₄C⁵ or Mo/B₄C.¹ In these 2 multilayer systems, the B₄C-on-metal interfaces were found more diffuse.

In the 3-layer model, we added an interdiffusion layer (IL-1) at the B₄C-on-Cr interface. Thus, the 3-layer model consists of a periodic stack with 3 layers per period: Cr, IL-1, and B₄C (see Fig. 2(a)). As shown in Fig. 1(b), the 3-layer model provides a more accurate fit of the relative intensities of the Bragg peaks and especially of the 2nd order Bragg peak.

We have used the same 3-layer model to fit the GIXR measurements of MS2, IBS1, and IBS2 samples. Concerning the 2 samples with very thin B₄C layers (MS3 and IBS3), the best fits were obtained with a 2-layer model made of Cr and IL-2 (see Fig. 2(b)). This indicates that all the sputtered B₄C is consumed to form the IL-2. Notice that this model is consistent with the IL-1 thickness values determined in samples

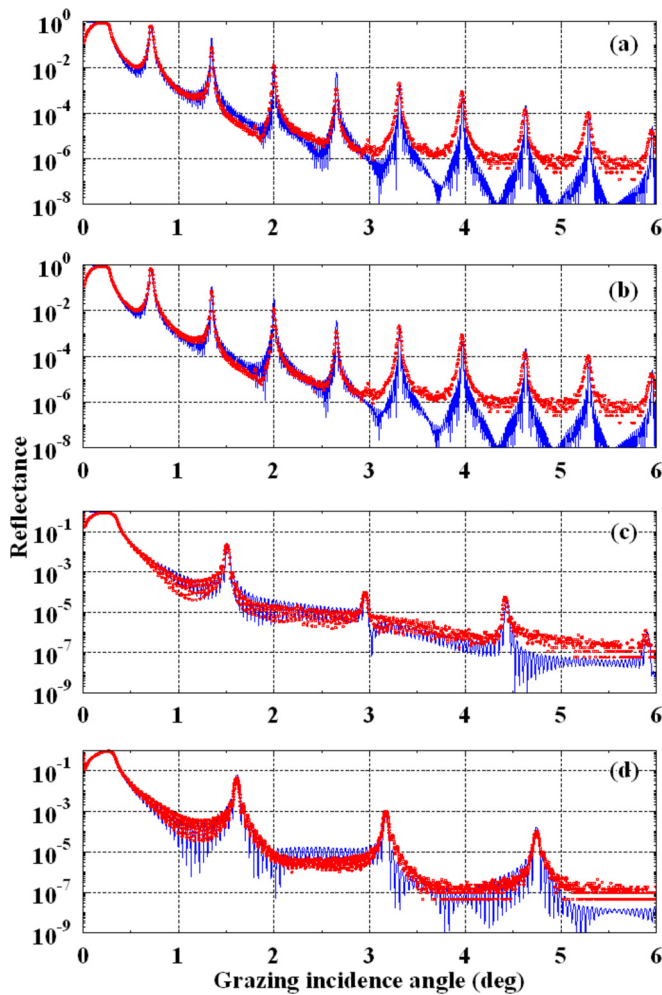


FIG. 1. GIXR measurements and fits for sample MS1 with (a) 2-layer (Cr/B₄C) model and (b) 3-layer (Cr/IL-1/B₄C) model, (c) sample MS3 with 2-layer (Cr/IL-2) model, and (d) sample IBS2 with 3-layer (Cr/IL-1/B₄C) model. The red points represent the experimental data, and the blue lines represent the fits.

with thicker B₄C layers. In this case, we suppose that the composition of the IL-2 may differ from IL-1 because the next Cr layer is deposited directly on the interfacial layer and not on a B₄C layer. The best fits were actually obtained for a layer IL-2 that contains more Cr than IL-1 (see Table I and Section II B). As examples of the above, we have plotted the experimental and fitted GIXR curves for sample MS3 (Fig. 1(c)) and IBS2 (Fig. 1(d)).

The results for samples MS1 (35 periods) and MS2 (10 periods) show that the IL thickness does not vary with the

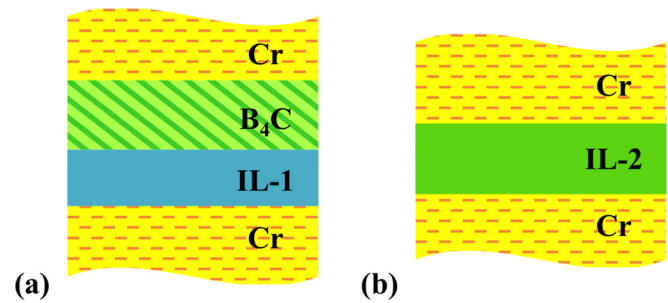


FIG. 2. Schematic of (a) the 3-layer Cr/IL-1/B₄C model and (b) Cr/IL-2 model.

number of periods in the stack. This is also true for the IBS samples: samples IBS1 (10 periods) and IBS2 (35 periods) present almost the same IL thickness. This means that the interdiffusion phenomena do not vary significantly during the deposition process (IBS or MS), and that these phenomena do not degrade the multilayer periodicity.

As reported in Table III, the IL appears to be present in all samples regardless of the deposition technique used (MS or IBS). However, the models indicate a slightly thinner IL in the case of IBS deposition: about 1 nm versus ≈ 1.5 nm for MS deposition. The interfacial roughness values determined by GIXR fits are quite low (between 0.2 and 0.4 nm rms) and are very similar for both deposition techniques. The surface roughness was measured by AFM on a $10 \times 10 \mu\text{m}^2$ area for all samples. For the MS samples, the rms roughness (σ_{rms}) ranges between 0.27 nm and 0.4 nm. For the IBS samples, σ_{rms} ranges between 0.24 nm and 0.35 nm. These results confirm that the surface of the Cr/B₄C multilayer coating is very smooth for all six samples. Moreover, the rms roughness values measured by AFM are consistent with the interfacial roughness values determined by GIXR and SXR fitting.

By comparing the targeted and fitted thickness values for MS1 and MS2 samples (see Tables II and III), we can estimate that approximately 1.7 nm of magnetron sputtered B₄C contribute to forming the IL with Cr. Thus, we expect that if the B₄C targeted thickness is thinner than 1.7 nm, all the sputtered B₄C will be used to form the IL. This is actually the case for sample MS3, which underlines the consistency of our model. Concerning the IBS samples, the fitted B₄C thickness for IBS1 and IBS2 samples is approximately 1 nm less than the targeted one. This value is also consistent with the fitted results for IBS3: the B₄C layer thickness in our 3-layer model goes to zero when the targeted B₄C thickness decreases from

TABLE III. Fitted multilayer parameters; units: nm, Th. = thickness, σ = roughness, and cap = capping layer.

Sample	Cr Th.	Cr σ	IL Th.	IL σ	B ₄ C Th.	B ₄ C σ	B ₄ C cap Th.	B ₄ C σ	B ₂ O ₃ Th.	B ₂ O ₃ σ
MS1 2-layer model	2.14	0.6	4.55	0.2	0.5	0.2
MS1 3-layer model	1.52	0.3	1.5	0.3	3.66	0.2	0.5	0.2
MS2	1.63	0.4	1.5	0.4	3.67	0.2	0.5	0.2
MS3	1.35	0.3	1.65	0.23	1.5	0.2
IBS1	2.47	0.4	1.1	0.4	2.35	0.27	1.7	0.3	0.6	0.25
IBS2	1.36	0.25	1.2	0.25	0.24	0.25	0.95	0.25	0.6	0.25
IBS3	1.28	0.35	1.09	0.28	0.9	0.3	0.6	0.3

1.2 nm (IBS2) to 0.7 nm (IBS3). These results show that the quantity of B_4C that is consumed to form the IL is about 1 nm and thus slightly lower in the case of ion beam sputtering compared to magnetron sputtering. This difference could be related to the energetics of the two deposition processes which may be leading to slightly different properties (density, stoichiometry, and crystallinity) of one or both materials (Cr and B_4C), and/or to slightly different interface mixing effects. In both MS and IBS samples, the total thickness of the IL appears to be approximately equal to the thickness of the B_4C layer that contributes to the IL.

The six samples ended with a B_4C top layer that has been shown earlier to oxidize in contact with air.³² The targeted top B_4C thickness was about 3 nm or thicker for all samples except MS3 (see Table II). We modeled the top oxide layer by adding a B_2O_3 thin film on top of the last B_4C layer, and we fitted its thickness. We found an oxide thickness in the range 0.5–0.6 nm for all samples (MS and IBS) except for sample MS3 that presents a thicker oxide layer (1.5 nm). The difference in oxide thickness for MS3 may be explained by the fact that the top layer in contact with air in this case is the interfacial layer IL-2 and not B_4C .

B. SXR measurements

The 3 samples with thicker periods (MS1, MS2, and IBS1) were characterized by $\theta/2\theta$ SXR measurements at photon energies around 170 eV at SOLEIL synchrotron. The results are plotted in Fig. 3.

The SXR data show a 1st Bragg peak at the expected angle position, consistent with the multilayer model parameters shown in Table III for each sample. MS1 and MS2 were measured at 172.4 eV and IBS1 at 170 eV. The difference between Bragg peak positions for samples MS2 and MS1 is due to a small difference in their multilayer period, again as evidenced by the layer model parameters derived in Table III for these two samples. The smaller period thickness of sample IBS1 and the difference in photon energy result in a shift of its Bragg peak towards greater grazing angles. Samples MS2 and IBS1 both have less bilayers ($N = 10$) than MS1

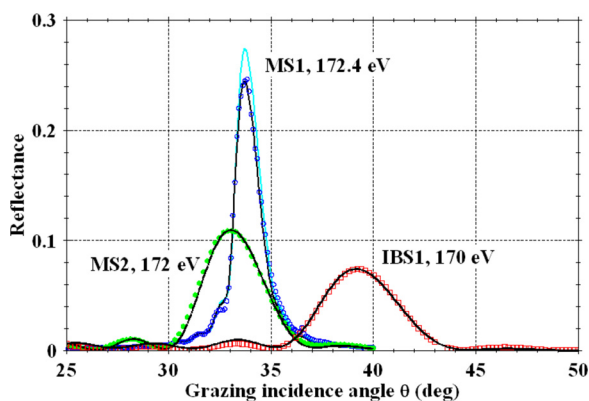


FIG. 3. Reflectance measurements (data points) obtained at SOLEIL synchrotron on three Cr/ B_4C multilayer samples are shown. A 3-layer model (Cr/IL-1/ B_4C , black solid line) is also plotted for each sample. The light blue solid line represents the best-fit 2-layer model (Cr/ B_4C) for the MS1 sample.

($N = 35$) leading to the observed differences in Bragg peak height and width.

Sample MS1 was also measured at beamline 6.3.2. of the ALS synchrotron at 172.4 eV photon energy. The x-ray beam at the ALS beamline was estimated to be about 90% s-polarized in this energy region, and this polarization value was used for all simulations at 170 and 172.4 eV. The measurements at both SOLEIL and ALS synchrotrons are consistent except for a slight angular shift (0.1°) between the two curves, which could be due to a sample alignment or photon energy calibration discrepancy between the two facilities. The peak reflectance values measured at ALS and at SOLEIL were, respectively, 24.2% and 24.6%.

In order to compare the performance of these 3 multilayers, we calculate the ratio between the measured reflectance and the “theoretical reflectance,” corresponding to the reflectance of a Cr/ B_4C multilayer stack with same period and thickness ratio, and ideal interfaces (no interface layer or interfacial roughness/interdiffusion). For samples MS2, MS1, and IBS1, we measured the peak reflectance values of 10.8%, 24.6%, and 7.4%, respectively; we obtain a ratio of, respectively, 0.725, 0.775, and 0.738. MS- and IBS-deposited Cr/ B_4C multilayers show thus similar reflective performance.

We have also plotted in Fig. 3 the fitted curves, calculated with the parameters given in Table III. For sample MS1, there is a significant difference in the peak reflectance between fits using the 2-layer (Cr/ B_4C) or the 3-layer model: 27.4% and 24.5%, respectively. With the 2-layer model, we were not able to fit accurately both the GIXR and SXR data, and the displayed fit is the best compromise that we achieved. On the other hand, the fits with the 3-layer model provide a very good agreement with the data for all three MS1, MS2, and IBS1 samples.

The fact that we were able to fit accurately the SXR and GIXR experimental data with the same set of parameters for each of the 3 samples confirms the validity of the 3-layer model.

The fact that the 3-layer model fits the data well both at around 170 eV and at 8 keV does not mean that there is no interdiffusion layer at the other interface (Cr-on- B_4C) in the Cr/ B_4C multilayer. However, it does indicate that if an interdiffusion layer exists at the Cr-on- B_4C interface it should be thinner, since it appears to be adequately represented by the “roughness/interdiffusion” parameter which is only 0.2 to 0.3 nm for this interface in our model.

As for the samples with thinner periods, we have performed SXR measurements at higher energies, in the vicinity of the Cr L edge. The angular reflectance spectrum of sample MS3 was measured at SOLEIL at a photon energy of 600 eV. This sample corresponds to a magnetron sputtered multilayer with very thin B_4C layers (see Table II). If we consider pure Cr and B_4C layers without any interdiffusion, we should expect from the simulation a peak reflectance of 4.5%. The experimental peak reflectance for sample MS3 is below 0.4%, and the noise level was about 0.1% for this measurement. The fact that the experimental peak reflectance is one order of magnitude lower than the theoretical one clearly indicates that extensive interdiffusion takes place

in this sample. Indeed, calculations using the Cr/IL-2 model (see Table II for model parameters) predict a peak reflectance value about 0.2% for this sample. We have obtained similar results on sample IBS3 deposited by ion beam sputtering. This sample was measured at SOLEIL at a photon energy of 574 eV. The reflectance vs. angle spectrum presents no Bragg peak between 20° and 30° grazing angle. Note that the noise level was relatively high (about 0.5%) due to relatively low photon flux on the beamline at this energy. The theoretical peak reflectance values for this sample are, respectively, 7% and 1.3% at 27° grazing angle for the Cr/B₄C and Cr/IL-2 models. Thus, for both samples MS3 and IBS3, the Cr/IL-2 multilayer model is in better agreement with experimental data than the Cr/B₄C model.

We have also measured the reflectance vs. angle spectrum of sample MS1 at 600 eV at SOLEIL. It presents a peak reflectance of 8.4% at 9.5° grazing angle. However, it was not possible to fit these experimental data with the tabulated Cr optical constants at this photon energy. Additional measurements were performed at ALS on this sample and will be discussed in Section III D.

C. HRTEM and STEM analyses

We selected two Cr/B₄C samples for the TEM study: sample MS1 that gives the highest reflectance at 170 eV and sample MS3 deposited with the same method but with much thinner B₄C layers.

Fig. 4 shows a bright-field TEM image obtained on sample MS1 displayed side-by-side with a STEM image of the same sample. They indicate a multilayer structure composed of homogeneous layers with smooth interfaces, as is also evidenced by the high reflectance of this sample discussed in Sections III A and III B. Fig. 5 shows a high-resolution TEM image obtained on sample MS3 displayed side-by-side with a STEM image. Although a periodic structure can be clearly seen across the entire multilayer in both TEM and STEM images, the layers appear somewhat inhomogeneous, and the

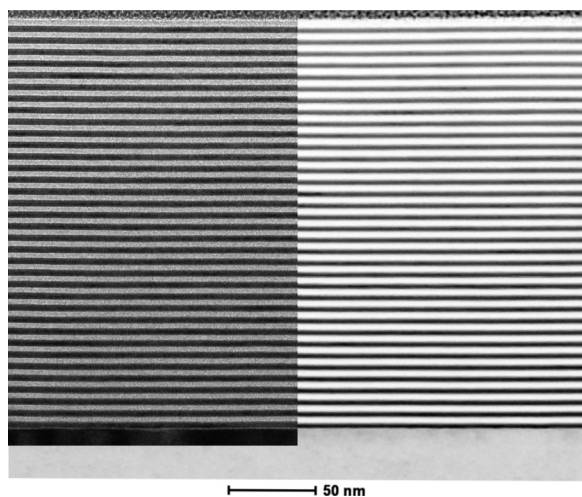


FIG. 4. Bright-field TEM image of sample MS1 obtained at 64 K magnification (left) is shown next to a STEM image obtained at 320 K magnification (right). The contrast of the STEM image has been inverted, to be in accord with the bright-field TEM image. Cr layers are shown as dark, while B₄C layers are shown as bright in the images.

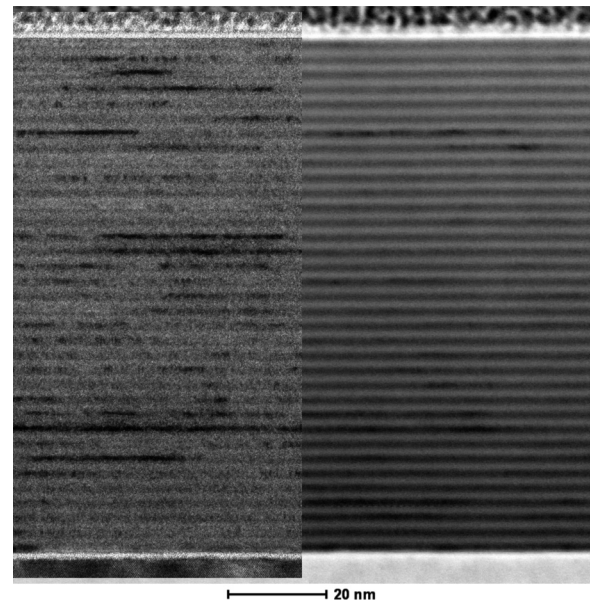


FIG. 5. High-resolution TEM image of sample MS3 obtained at 180 K magnification (left) is shown next to a STEM image obtained at 900 K magnification (right). The contrast of the STEM image has been inverted, to be in accord with the bright-field TEM image. Cr layers are shown as dark, while B₄C-containing layers are shown as bright in the images.

contrast between them is reduced. The appearance of the B₄C layers in Figs. 4 and 5 suggests that the B₄C layers are most likely amorphous, as already reported previously.^{5,13,32} It is possible that the Cr layers may be polycrystalline, based on the presence of darker areas within the Cr-containing layers in Figs. 4 and 5, which could be attributed to the presence of crystallites. A detailed study of the morphology and microstructure of the B₄C and Cr layers inside these multilayers is currently underway and will be included in a future publication. The intensity profiles extracted from the TEM/STEM images in Figs. 4 and 5 are shown in Figs. 6(a) and 7, respectively. For sample MS1, we have also plotted the profiles obtained from TEM and STEM images with higher magnifications (Fig. 6(b)). The profiles in Fig. 7 (sample MS3) clearly demonstrate the absence of sharply defined layers. These imaging results are consistent with the 8 keV data and model from sample MS3 (see Table III), in which the very thin B₄C layer is entirely consumed into an interdiffusion layer (IL-2). It is worthwhile noting the good qualitative agreement between the TEM and STEM profiles in both MS1 and MS3 samples.

The TEM image intensity profile of sample MS1 in Fig. 6(b) shows a regularly distributed periodic structure with the maxima representing B₄C layers and the minima representing Cr layers. One can observe some “bumps” at the B₄C-on-Cr interfaces, which coincide with the interfacial layer of our model (IL-1). One can also note the presence of bumps at the other interface (Cr-on-B₄C), but those bumps are smaller, which again tends to validate our 3-layer model.

The layer thicknesses in sample MS1 have been estimated using TEM image intensity profiles. The method that was used is the following: The points corresponding to the position of the Cr layers (minima), the center of the B₄C layers (center of the “B₄C plateau”), and the bumps and dips

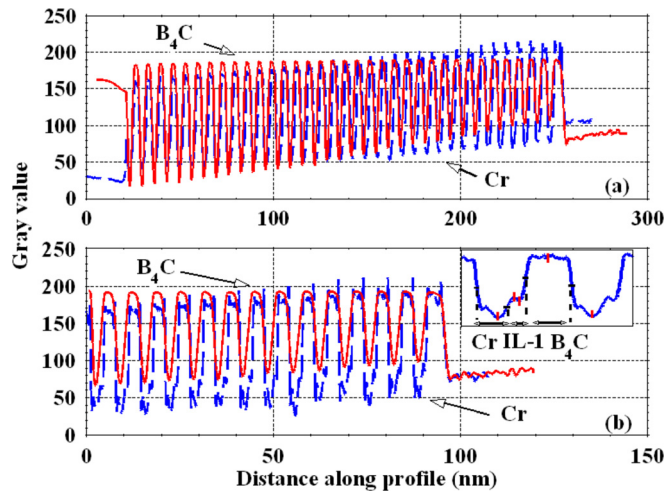


FIG. 6. (a) Superimposed profiles of the bright-field TEM image at 64 K magnification (dashed blue line) and STEM image at 320 K magnification (solid red line) shown in Fig. 4 for sample MS1. (b) Superimposed profiles of a bright-field TEM image at 180 K magnification (dashed blue line) and STEM image at 900 K magnification (solid red line) of sample MS1. The substrate (not shown) is on the left hand side of the plot, and the nearly constant line on the right hand side is the platinum coating used for TEM preparation at the top of the multilayer. The inset shows a profile extracted from a high-resolution TEM image of sample MS1 obtained at 255 K magnification, demonstrating the method that was used for layer thickness estimation.

corresponding to interdiffusion layer IL-1 were manually selected (see red vertical strokes in the inset of Fig. 6(b)). The points corresponding to the layer boundaries (see black horizontal strokes and black dash lines in the inset of Fig. 6(b)) were then calculated so that they were at half height between the previously selected points.

The averaged values for layer thicknesses in sample MS1 determined with the above method are the following: 2.17 nm for Cr, 1.36 nm for IL-1, and 3.13 nm for B_4C , with an average measured period of 6.68 nm. These results are compatible with our model, showing an IL-1 thickness close to 1.5 nm.

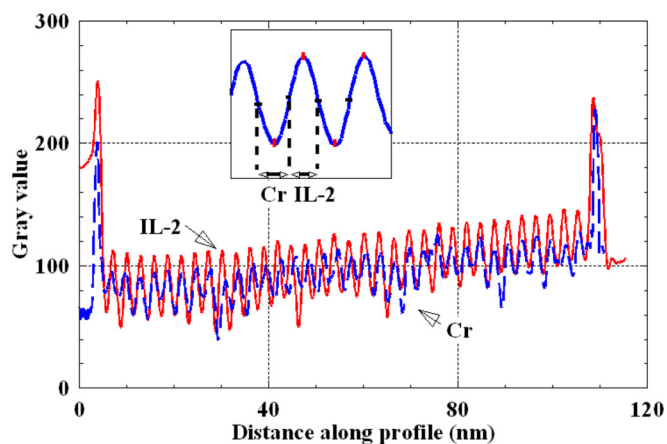


FIG. 7. Superimposed profiles of the high-resolution TEM image at 180 K magnification (dashed blue line) and STEM image at 900 K magnification (solid red line) shown in Fig. 5 for sample MS3. The substrate can be seen on the left hand side at the beginning of the curve, and the platinum coating used for TEM preparation at the top of the multilayer is on the right hand side. The inset shows a detail from the STEM profile at 900 K, demonstrating the method that was used for layer thickness estimation.

The same method was employed to determine the layer thicknesses in sample MS3. Here, a 2-layer model was used (Cr/IL-2), as discussed earlier. The layer thicknesses were estimated using the STEM image intensity profile, since it is less noisy than the TEM intensity profile (see Fig. 7). We selected the minima and maxima corresponding to Cr and IL-2 layers (see red strokes in the inset of Fig. 7) and then calculated the position of the layer boundaries (see black horizontal lines and black dash lines in the inset of Fig. 7) given by the positions corresponding to half height between the previous points.

In this manner, the averaged values for layer thicknesses in sample MS3 were found to be 1.42 nm for Cr and 1.57 nm for IL-2, with an average period of 2.98 nm. These values are close to those of the model we obtained from the 8 keV and SXR measurements (see Table III).

D. Reflectance measurements in the vicinity of the Cr $L_{2,3}$ absorption edge

Fig. 8 shows the reflectance vs. photon energy measurements performed on sample MS1 in the vicinity of the Cr $L_{2,3}$ absorption edge, at incidence angles ranging from 8.6° to 9.6° . As expected, the peak reflectance increases when the peak gets closer to the absorption edge and the peak becomes narrower. One can notice that a smaller peak is present on all curves around 585 eV and that its position is independent on the grazing angle. Fig. 9 shows the measured curve with the highest peak reflectance, 51.5% at 572.94 eV, obtained at 9.2° grazing incidence angle. The 3-layer model (see parameters in Table III) using the available optical constants for Cr³³ is also plotted for comparison. The agreement between the model and the data is poor. Especially, the peak around 585 eV in the measurements cannot be reproduced by the model. This feature, attributed to the Cr L_2 absorption edge, is evidently missing from the tabulated optical constants, thus indicating lack of accurate Cr optical constants' values around the $L_{2,3}$ edge.

We have also measured the reflectance vs. incidence angle at 572.94 eV and 600 eV at ALS on sample MS1. These measurements demonstrated up to 3 orders of

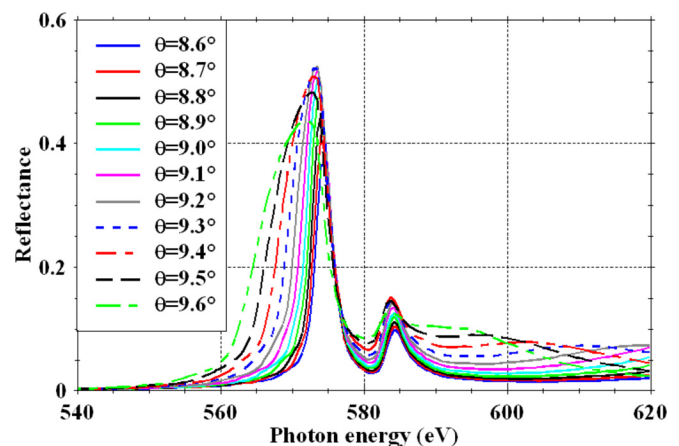


FIG. 8. Reflectance vs. photon energy measurements on sample MS1 obtained at ALS beamline 6.3.2. are shown, for grazing incidence angles in the range 8.6° to 9.6° .

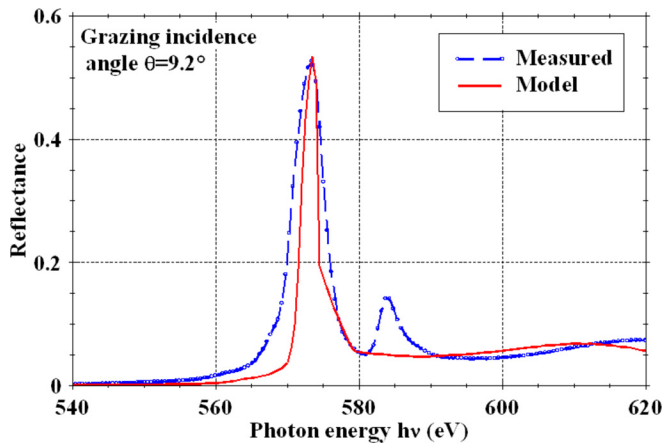


FIG. 9. Reflectance vs. photon energy measurements on sample MS1 obtained at ALS beamline 6.3.2. are plotted with a best-fit, 3-layer model. The discrepancy between model and data is attributed to lack of accurate optical constants in the vicinity of the Cr $L_{2,3}$ edge. The secondary peak to the right of the main Bragg peak in the data is attributed to the Cr L_2 edge.

well-defined Bragg peaks, which confirm the quality of this multilayer. Fig. 10 shows the data at 600 eV and the reflectance calculated with the 3-layer model (see parameters in Table III). Once again, there is significant disagreement between the experimental data and the calculation using available Cr optical constants. The critical angle and the shape and location of the Bragg peaks are not well reproduced by the simulation. We have also plotted in Fig. 10 the reflectance calculated by using the 3-layer model (same parameters as previously, see Table III) and by fitting the optical constants of Cr. The fitted values of the Cr optical constants are displayed in Fig. 10 and compared to Henke data.³³ One can notice the very good agreement between the experimental data and the fitted curve. These results confirm the validity of the 3-layer model for Cr/ B_4C multilayers and provide new values of Cr optical constants at 600 eV, with the greatest difference being in the delta value as compared to previously available data. We applied the same procedure

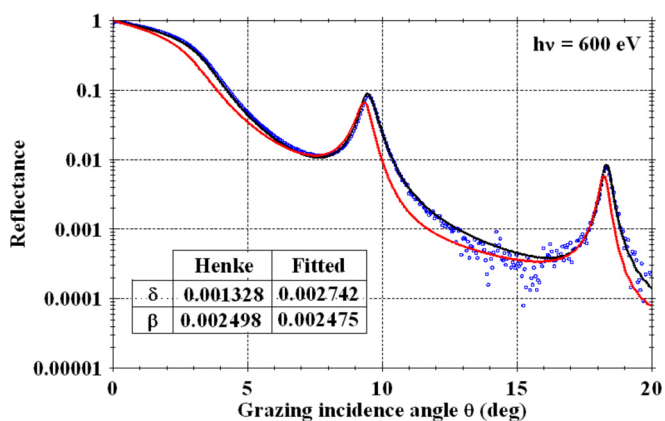


FIG. 10. Reflectance vs. incidence angle measurements obtained at ALS beamline 6.3.2. at 600 eV are shown. A best fit using the 3-layer model (Cr/IL-1/ B_4C) and the tabulated optical constants for Cr (red solid line) is shown. Another best-fit, using the same model but with the Cr optical constants δ , β , as fitting parameters (solid black line), is also shown. The fitted values for the Cr optical constants are also given in the inset and compared with the tabulated (Henke) values.³³

with the experimental reflectance data at 572.94 eV (not shown here) and obtained: -0.003713 (δ) and 0.0005701 (β), as compared to -0.002509 (δ) and 0.0003354 (β) from the Henke tables.

IV. CONCLUSIONS

We have deposited by magnetron sputtering and ion beam sputtering a set of periodic Cr/ B_4C multilayer mirrors. We obtained GIXR and SXR measurements at photon energies ranging from 8 keV down to 172 eV and fitted the results. Our fits worked consistently at all measured photon energies and revealed the presence of asymmetric interfaces within the Cr/ B_4C multilayer structure, with a 1–1.5 nm thick interdiffusion layer at the B_4C -on-Cr interface, which was included in a 3-layer multilayer model. The multilayers with very thin (about 1 nm) B_4C layers showed very low X-ray reflectance and were fitted consistently with a 2-layer multilayer model, composed of only Cr and interdiffusion layers.

These conclusions are also supported by TEM and STEM analyses. The results reported in this paper enhance the optimization of Cr/ B_4C multilayer performance and the understanding of the physics of ultra-short-period Cr/ B_4C multilayers and B_4C barrier layers in Cr-based multilayers. Cr/ B_4C multilayer coatings have already been optimized using the 3-layer model proposed here and deposited to produce an alternate multilayer grating that acts as a high efficiency monochromator for synchrotron radiation between 1 and 4 keV.

Finally, we report on Cr/ B_4C reflectance measurements in the vicinity of the Cr $L_{2,3}$ absorption edge, which reveal features that are not predicted by the tabulated optical constants of Cr. By fitting reflectance vs. angle scans at 572.94 eV and at 600 eV, we have determined new values of Cr optical constants at these energies that differ significantly from the Henke tables. These results demonstrate the need for accurate Cr optical constants' measurements at photon energies close to the Cr $L_{2,3}$ absorption edge. This would enable a more accurate performance optimization of Cr/ B_4C and of other Cr-based multilayer systems that operate in this spectral domain, thus unlocking their full potential.

ACKNOWLEDGMENTS

The authors would like to thank Santhosh Chenna and Lancy Chung (EAG Labs) for assistance with the TEM image acquisition. MS samples have been deposited as part of CEMOX (Centrale d'Elaboration et de Métrologie d'Optique X), a platform of LUMAT federation (CNRS FR2764). This work was partly supported by the French Research Agency under Contract Nos. ANR-11-EQPX-0029 and ANR-10-LABX-0039. This work was performed under the auspices of the U.S. Department of Energy by Lawrence Livermore National Laboratory (LLNL) under Contract No. DE-AC52-07NA27344 and by the University of California Lawrence Berkeley National Laboratory under Contract No. DE-AC03-76F00098. Funding was provided in part by LLNL's Professional Research and Teaching Leave Program.

- ¹F. Choueikani, B. Lagarde, F. Delmotte, M. Krumrey, F. Bridou, M. Thomasset, E. Meltchakov, and F. Polack, *Opt. Lett.* **39**, 2141 (2014).
- ²F. Christensen, Z. Shou-Hua, A. Hornstrup, H. Schnopper, and J. W. P. Plag, *J. X-Ray Sci. Technol.* **3**, 1 (1991).
- ³D. L. Windt, E. M. Gullikson, and C. C. Walton, *Opt. Lett.* **27**, 2212 (2002).
- ⁴N. I. Chkhalo, S. Künstner, V. N. Polkovnikov, N. N. Salashchenko, F. Schäfers, and S. D. Starikov, *Appl. Phys. Lett.* **102**, 011602 (2013).
- ⁵C. Michaelsen, J. Wiesmann, R. Bormann, C. Nowak, C. Dieker, S. Hollensteiner, and W. Jäger, *Opt. Lett.* **26**, 792 (2001).
- ⁶S. S. Andreev, A. D. Akhsakhalyan, M. A. Bibishkin, N. I. Chkhalo, S. V. Gaponov, S. A. Gusev, E. B. Kluev, K. A. Prokhorov, N. N. Salashchenko, F. Schäfers, and S. Y. Zuev, *Cent. Eur. J. Phys.* **1**, 191 (2003).
- ⁷Y. Y. Platonov, L. Gomez, and D. Broadway, *Proc. SPIE* **4782**, 152 (2002).
- ⁸I. A. Makhotkin, E. Zoethout, E. Louis, A. M. Yakunin, S. Millender, and F. Bijkerk, *Opt. Express* **20**, 11778 (2012).
- ⁹D. G. Stearns, S. P. Vernon, and R. S. Rosen, *Opt. Lett.* **16**, 1283 (1991).
- ¹⁰C. Montcalm, P. A. Kearney, J. M. Slaughter, B. T. Sullivan, M. Chaker, H. Pepin, and C. M. Falco, *Appl. Opt.* **35**, 5134 (1996).
- ¹¹P. Boher, P. Houdy, P. Kaikati, R. J. Barchewitz, L. J. Van Ijzendoorn, Z. Li, D. J. Smith, and J. C. Joud, *Proc. SPIE* **1345**, 165 (1991).
- ¹²A. E. Yakshin, I. I. Khodos, I. M. Zhelezniak, and A. I. Erko, *Opt. Commun.* **118**, 133 (1995).
- ¹³C. Borchers and C. Michaelsen, *Philos. Mag. A* **82**, 1195 (2002).
- ¹⁴A. F. Jankowski and P. L. Perry, *Thin Solid Films* **206**, 365 (1991).
- ¹⁵R. Dietsch, S. Braun, T. Holz, H. Mai, R. Scholz, and L. Brügemann, *Proc. SPIE* **4144**, 137 (2000).
- ¹⁶J. M. Slaughter, R. N. Watts, C. M. Falco, C. Tarrío, B. S. Medower, and T. B. Lucatorro, *Opt. Lett.* **19**, 1786 (1994).
- ¹⁷J. Gautier, F. Delmotte, M. Roulliay, F. Bridou, M.-F. Ravet, and A. Jérôme, *Appl. Opt.* **44**, 384 (2005).
- ¹⁸E. Meltchakov, C. Hecquet, M. Roulliay, S. De Rossi, Y. Menesguen, A. Jérôme, F. Bridou, F. Varniere, M.-F. Ravet-Krill, and F. Delmotte, *Appl. Phys. A* **98**, 111 (2010).
- ¹⁹F. Comin, G. Apostolo, A. K. Freund, P. Mangiagalli, M. Navizet, and C. L. Troxel, *Proc. SPIE* **3448**, 11 (1998).
- ²⁰E. M. Gullikson, F. Salamassi, A. L. Aquila, and F. Dollar, "Progress in short period multilayer coatings for water window applications," presented at the 8th International Conference on the Physics of X-Ray Multilayer Structures (PXRMS), oral presentation, Sapporo, Japan (2006), see also <http://escholarship.org/uc/item/8hv7q0hj>.
- ²¹H.-E. Schaefer, *Nanoscience: The Science of the Small in Physics, Engineering, Chemistry, Biology and Medicine* (Springer-Verlag, Berlin Heidelberg, 2010).
- ²²M. Prasciolu, A. F. G. Leontowich, K. R. Beyerlein, and S. Bajt, *Appl. Opt.* **53**, 2126 (2014).
- ²³H. Jiang, A. G. Michette, S. J. Pfauntsch, D. Hart, and M. Shand, in *Proceedings of PIERS* (Xi'an, China, 2010), pp. 61–65.
- ²⁴F. Bridou, F. Delmotte, P. Troussel, and B. Villette, *Nucl. Instrum. Methods Phys. Res., Sect. A* **680**, 69 (2012).
- ²⁵Z. Zhang, Y. Liang, W. Li, Z. Wang, and H. Chen, *Thin Solid Films* **531**, 302 (2013).
- ²⁶A. Ziani, F. Delmotte, C. Le Paven-Thivet, E. Meltchakov, A. Jérôme, M. Roulliay, F. Bridou, and K. Gasc, *Thin Solid Films* **552**, 62 (2014).
- ²⁷M. Idir, P. Mercere, T. Moreno, and A. Delmotte, *Synchrotron Radiat. News* **19**, 18 (2006).
- ²⁸J. H. Underwood and E. M. Gullikson, *J. Electron Spectrosc. Relat. Phenom.* **92**, 265 (1998).
- ²⁹E. M. Gullikson, S. Mrowka, and B. B. Kaufmann, *Proc. SPIE* **4343**, 363 (2001).
- ³⁰R. Soufli, M. Fernández-Perea, S. L. Baker, J. C. Robinson, E. M. Gullikson, P. Heimann, V. V. Yashchuk, W. R. McKinney, W. F. Schlotter, and M. Rowen, *Appl. Opt.* **51**, 2118 (2012).
- ³¹D. L. Windt, *Comput. Phys.* **12**, 360 (1998), see also <http://www.rxoll.com/idl/>.
- ³²R. Soufli, A. L. Aquila, F. Salamassi, M. Fernández-Perea, and E. M. Gullikson, *Appl. Opt.* **47**, 4633 (2008).
- ³³B. Henke, E. Gullikson, and J. Davis, *At. Data Nucl. Data Tables* **54**, 181 (1993), see also http://henke.lbl.gov/optical_constants/.